



1                   **A NEW LAGRANGIAN BASED SHORT TERM PREDICTION**  
2                   **METHODOLOGY FOR HF RADAR CURRENTS**

3

4   Lohitzune Solabarrieta<sup>1,2</sup>, Ismael Hernandez-Carrasco<sup>3</sup>, Anna Rubio<sup>4</sup>, Alejandro Orfila<sup>3</sup>, Michael  
5   Campbell<sup>1</sup>, Ganix Esnaola<sup>5,6</sup>, Julien Mader<sup>4</sup>, Burton H. Jones<sup>1</sup>.

6

7   (1) KAUST, Red Sea Research Center, Integrated Ocean Processes, Saudi Arabia.

8   (2) Mondragon Unibertsitatea, Faculty of Engineering, Electronics and Computer Science  
9   department, Loramendi 4, Mondragon 20500 Gipuzkoa, Spain

10   (3) Instituto Mediterráneo de Estudios Avanzados. IMEDEA (CSIC-UIB), 07190 Esporles, Spain.

11   (4) AZTI Marine Research, Pasaia, Spain

12   (5) Nuclear Engineering and Fluid Mechanics Dept., Gipuzkoako Ingeniaritza Eskola, Europa  
13   Plaza 1, 20018-Donostia, Spain.

14   (6) Joint Research Unit BEGIK, Instituto Español de Oceanografía (IEO)-Universidad del País  
15   Vasco/Euskal Herriko Unibertsitatea (UPV/EHU), Plentziako Itsas Estazioa, Areatza  
16   Pasealekua, 48620-Plentzia, Spain

17

18

19   Corresponding author's email: lohitzune.solabarrieta@kaust.edu.sa



20 **ABSTRACT**

21

22 The use of High Frequency Radar (HFR) data is increasing worldwide for  
23 operational oceanography and data assimilation, as it provides real-time coastal  
24 surface currents at high temporal and spatial resolution. In this work, a Lagrangian  
25 based empirical real-time, Short-Term Prediction (L-STP) system is presented in  
26 order to provide short term forecasts of up to 48 hours of ocean currents from HFR  
27 data. The method is based on the finding of historical gridded analogues of  
28 Lagrangian trajectories obtained from HFR surface currents. Then, assuming that  
29 the present state will follow the same temporal evolution as did the historical  
30 analogue, we obtain a short-term prediction of the surface currents. The method is  
31 applied to two HFR systems covering two areas with different dynamical  
32 characteristics: the southeast Bay of Biscay and the central Red Sea. The L-STP  
33 improves on previous prediction systems implemented for the SE Bay of Biscay and  
34 provides good results for the Red Sea study area. A comparison of the L-STP  
35 methodology with predictions based on persistence and reference fields has been  
36 performed in order to quantify the error introduced by this Lagrangian approach.  
37 Furthermore, a temporal sensitivity analysis has been addressed to determine the  
38 limit of applicability of the methodology regarding the temporal horizon of  
39 Lagrangian prediction. A real-time skill-score has been developed using the results  
40 of this analysis which allows to identify periods when the short-term prediction  
41 performance is more likely to be low and persistence can be used as a better predictor  
42 for the future currents.



43 **1. INTRODUCTION**

44 The coastal zone is experiencing increased human pressure. On the one hand, during  
45 recent decades coastal seas have been experiencing increased activity for recreation,  
46 transport, fisheries and marine-related energy production. Simultaneously,  
47 continued growth of the global coastal population largely contributes to increase the  
48 problem of the wastewater discharge which, in many cases, results in serious damage  
49 to coastal marine ecosystems. Thus, to understand and manage these regions, and to  
50 evaluate water quality and control the dynamical processes occurring near the  
51 shoreline and close offshore, the demand for real time, operational monitoring of the  
52 coastal ocean has exploded. These processes are responsible of the transport and fate  
53 of pollutants, nutrients, jellyfish, harmful algal blooms, plastics, etc, and a better  
54 knowledge of these processes is necessary to identify regions of accumulation or  
55 dispersion of these harmful materials. This requirement is driving the set-up of a  
56 growing number of multi-platform operational observing systems designed for the  
57 continuous monitoring of the coastal ocean (e.g., US IOOS, EU EOOS, SOCIB,  
58 Australian IMOS, etc.). In the need of providing a long-term framework for the  
59 development and improvement of the European Marine coastal observations, the  
60 JERICO-NEXT project has been putting efforts to develop methods and tools for the  
61 production of high-quality marine data, and the sharing of expertise and  
62 infrastructures between the exiting observatories in Europe. Moreover, due to the  
63 need of forecasting applications for response to emergency situations such oil spills,  
64 or search and rescue operations, many of the existing operational observatories are  
65 linked with operational ocean forecasting models with or without data assimilation  
66 (e.g. MARACOOS, NOAA Global Real-Time Ocean Forecast System,  
67 COPERNICUS Marine Environment Monitoring System). Typically, constituted  
68 with different in-situ point-wise observational platforms (such as moored buoys,



69 tidal gauges, wave buoys, etc.) a significant number of these observatories now  
70 employ land-based High Frequency Radars (HFR), that provide real-time coastal  
71 currents with unprecedented coverage and resolution (e.g. Paduan and Rosenfeld,  
72 1996; Kohut and Glenn, 2003; Abascal et al., 2009; Solabarrieta et al., 2014, Rubio  
73 et al. 2017; Paduan and Washburn, 2013). Each HFR coastal site measures radial  
74 surface currents moving away or approaching its land-based antenna, based in the  
75 shift of the first peak of the Doppler spectra (Crombie 1955, Barrick et al 1977).  
76 Combining the overlapping radial vectors from at least 2 antennas provides surface  
77 true vector currents (Barrick et al., 1977, Lipa and Barrick, 1983). Several studies  
78 have compared in-situ current measurements with HFR observations (e.g., Schott et  
79 al. 1985; Hammond et al. 1987; Paduan and Rosenfeld 1996, Emery et al. 2004;  
80 Paduan et al., 2006; Ohlmann et al. 2007; Liu et al., 2014; Solabarrieta et al, 2014,  
81 Bellomo et al., 2015; Lana et al., 2016; Hernandez-Carrasco et al., 2018b) and have  
82 repeatedly demonstrated the validity of this technology. Presently, more than 250  
83 HFR antennas are installed being active worldwide (Roarty et al., 2019;  
84 <http://global-hfradar.org/>).

85

86 The range and the spatial resolution of the HFR current systems depend on their  
87 working frequency and the conductivity of the water over which the system is  
88 measuring. Ranges vary from 15 to 220 km range and spatial resolution from 250 m  
89 to 12 km. Typically, a 12 MHz radar has a range ~70 km with a spatial resolution of  
90 2-5 km. HFR systems usually average current measurements for one hour, although  
91 some average currents for shorter periods, such as 30 minutes. Due to their high  
92 spatio-temporal resolution, HFR data are commonly used in real time for search and  
93 rescue (Ullman et al., 2006) or oil spill prediction/mitigation emergency response  
94 (Abascal et al., 2017).

95



96 The performance of HFR for measuring near-real time surface currents has resulted  
97 in the development of assimilation strategies that incorporate the HFR measured  
98 surface currents into ocean coastal models (Breivik and Saetra, 2001, Oke et al 2002,  
99 Paduan and Shulman 2004, Stanev et al., 2011, Barth et al., 2011) some of which  
100 have been tested for short periods of time (Chao et al., 2009). However, assimilation  
101 of HFR data into models is still a computationally expensive and complex issue, not  
102 to mention operational applications of such a procedure. Because of these  
103 constrains, the availability of real-time high-resolution HFR current fields has led to  
104 alternative solutions in order to obtain short term prediction (STP) of coastal  
105 currents, through the direct use of HFR historical and nowcast observations using  
106 different approaches (e.g. Zelenke 2005, Frolov et al. 2011, Barrick et al., 2012,  
107 Orfila et al. 2015, Solabarrieta et al. 2016, Vilibić et al, 2016, Ren et al., 2019). The  
108 main characteristics of these STP approaches are summarized in Table 1.

109

110 The above-mentioned studies develop and implement different STP approaches  
111 (harmonic analysis of the last hours, genetic algorithms, numerical models, ...)  
112 which often require additional data, or long training periods of data without gaps  
113 which can jeopardize the general utility of these methods in real time.

114

115 Hardware failures due to power issues, communications or environmental conditions  
116 often result in spatio-temporal gaps within HFR datasets. Spatial gaps can be filled  
117 on a real-time basis but the filling of long temporal gaps is not straightforward.  
118 Several gap-filling methodologies have been developed for HFR data sets: Open  
119 Modal Analysis, (OMA) (Kaplan and Lekien, 2007), Data Interpolating EOFs  
120 (DINEOF) (Hernandez-Carrasco et al., 2018), and Self-Organizing Maps (SOM)  
121 (Hernandez-Carrasco et al., 2018). The OMA method has been used for spatial gap



122 filling in this paper because it is easily applied on real time data with available codes  
123 and it has well demonstrated results (Kaplan and Lekien, 2007).

124

125 A widely used method in time series prediction, especially in early weather  
126 forecasting, is the method of analogues. It is based on the assumption that if the  
127 behavior of a system at a given time is similar to some other situation in the historical  
128 record, then the evolution in the future of state will be similar to the evolution  
129 observed in the same historical record. Simply stated, two analogue fields are two  
130 distinct fields that are close enough considering some metric, to be considered as  
131 equivalent. The finding of the best (nearest) analogue of a specific time does not  
132 require a historically continuous dataset, as long as it contains subsets of  
133 observations that extend longer than the testing period. These analogue events occur  
134 naturally in the environment and this methodology has been applied and tested in  
135 atmospheric forecasts (Lorenz, 1969, Jianping et al, 1993, Prince and Goswami 2007,  
136 Shao and Li 2013).

137

138 Lagrangian computations have proven to be robust in identifying dynamical flow  
139 structures. Also, the Lagrangian description provides a more complete description  
140 of the dynamical processes involved in the transport of tracers, for example those  
141 deriving from the interaction of mesoscale structures, such as sub-grid filaments  
142 formed by eddy-eddy interaction, which cannot be captured directly from the  
143 Eulerian velocity field. This is due to the exploratory capacity of the flow along the  
144 trajectory history. We believe that using this approach, we will capture additional  
145 dynamical features present in the flow that are not readily apparent in pure velocity  
146 fields. Thus, improving the selection of a more appropriate analogue candidate.

147



148 Given the motivation described above, and developed partially in the framework of  
149 JERICO-NEXT project, we present a simple Lagrangian-based Short-Term  
150 Prediction (L-STP from now on) methodology using existing HFR datasets, to be  
151 applied to current real-time observations. The uniqueness of this approach is two-  
152 fold: first the historical Eulerian velocity fields are used to construct a catalogue of  
153 Lagrangian trajectories and second, using the trajectories obtained from present  
154 observations, analogues in the past dataset are searched in order to obtain the best  
155 predictive match. This new real-time Lagrangian based short-term prediction  
156 methodology is intended to be implemented operationally requiring low  
157 computational cost and is easy to implement using existing HFR data processing  
158 tools.  
159



160 **2. DATA AND METHODS**

161 *2.1 Data*

162 HFR data from two distinct oceanographic regions have been used for the  
163 evaluation, validation and testing of the developed methodology in this paper (Figure  
164 1): Left: The Bay of Biscay (hereinafter BoB HFR) and Right: The central Red Sea  
165 region (hereinafter Red Sea HFR). These two study regions are used to evaluate the  
166 skill of the method with different dynamical conditions, and with a sufficient set of  
167 observations to provide a database from which to find appropriate analogues. The  
168 BoB HFR system, located in the southeastern corner of the Bay of Biscay, in the  
169 Basque Country, is composed of two CODAR Seasonde sites, working since 2009  
170 which transmit at 4.5MHz frequency covering up to 200km range and providing  
171 hourly surface velocity field at 5 km of spatial resolution. The dataset used in this  
172 study spans the period from 2012 to 2015. The Red Sea HFR system is located on  
173 the central western coast of Saudi Arabia and is also composed of two CODAR  
174 Seasonde sites, operational since June 2017, transmitting at 16.12MHz frequency,  
175 covering up to 120 km range and providing the hourly surface velocity field at 3 km  
176 spatial resolution. The dataset from June 2017 to October 2018 has been used in this  
177 study.

178

179 The BoB HFR has been chosen as the pilot system for testing the developed  
180 methodology because of our previous knowledge regarding the circulation and  
181 dynamical processes in the study area (Rubio et al 2013, Solabarrieta et al 2014,  
182 Solabarrieta et al., 2015, Rubio et al., 2018, Hernandez-Carrasco et al. 2018). The  
183 resulting methodology is then applied to the operational Red Sea HFR dataset, as a  
184 study case. Coastal dynamics in the BoB show a clear seasonality where cyclonic  
185 and anticyclonic eddies dominate in winter and summer, respectively in responding



186 to local winds and the mean coastal current (Iberian Poleward Current) (Esnaola et  
187 al., 2013, Solabarrieta et al., 2014). The circulation in the area covered by the central  
188 Red Sea HFR also demonstrates a clear seasonality (Sofianos and Johns, 2003; Yao  
189 et al., 2014a, 2014b; Zarokanellos et al., 2016, 2017) linked to the seasonal winds of  
190 the area (Abualnaja et al., 2014; Langodan et al., 2017). The region is dominated by  
191 eddy activity, with both cyclonic and anticyclonic eddies dominating the region  
192 (Zhan et al., 2014; Zarokanellos et al. 2016). Due to the only recently available  
193 dataset (since mid-June 2017 to present) the detailed small-scale surface circulation  
194 processes of this area is under characterization at the moment.

195

196 The primary difference between the two HFR systems is the operating frequency  
197 (5MHz for the BoB system and 16 MHz for the Red Sea system) resulting in a larger  
198 spatial coverage for the BoB HFR than for the Red Sea HFR (200km range vs.  
199 120km, respectively), but with higher spatial resolution for the Red Sea HFR than  
200 for BoB HFR (3km and 5 km, respectively). This difference in the spatial resolution  
201 should result in better capturing the small-scale dynamical features in the Red Sea  
202 that could influence in the selection of an analogue.

203

204 The data from both systems have been processed similarly. The spectra of the  
205 received backscattered signal are converted into radial velocities using the MUltiple  
206 Signal Classification (MUSIC) algorithm (Schmidt 1986). HFR Progs MATLAB  
207 package (<https://cencalarchive.org/~cocmpmb/COCMPwiki>) is then used to  
208 combine radial currents and generate gap-filled total 2D currents, using the Open  
209 Modal Analysis (OMA) methodology of Kaplan and Lekien (2007).

210



211        *2.2 Lagrangian analogues*

212        The proposed methodology is based on the Lagrangian analogue finding approach,  
213        using the historical catalogue of trajectories and finding the most similar one of the  
214        last 48 hours. The method embeds trajectories of particles in a state space using delay  
215        coordinates. Analogue finding has been applied in several geophysical variables in  
216        different regions (Zorita and von Storch, 1999; Fernandez-Ferrero et al., 2009, 2010;  
217        Ibarra-Berastegi et al., 2011; Martin et al., 2014; Seubert et al., 2014; Ibarra-  
218        Berastegi et al., 2015).

219

220        The idea behind the methodology is to search the historical Lagrangian trajectories  
221        dataset for the field that best matches the previous 48-hour trajectory field (target  
222        field) and use it as the closest, chosen analogue. Then, the future time evolution of  
223        the analogue provides the forecast for the present case. In other words, if we find a  
224        state in the historical database that is close enough to the target period (given a  
225        metric), the forecast for the current observations will evolve in the same way as did  
226        the historical chosen period.

227

228        The analogue finding was first applied to surface velocity fields of the BoB HFR  
229        System, but the results did not improve the previously published STP results for the  
230        study area. The methodology was later tested with a four-year BoB dataset (2012-  
231        2015) where the trajectory fields belonging to the three first years are used as the  
232        search catalogue for analogues (2012-2014) (hereinafter “Lagrangian catalogue”),  
233        and the remaining year (2015) used as a test case (hereinafter “test period”) from  
234        where we extract the last 48-hour’s target trajectories (hereinafter “target field”)   
235        every hour (excluding the last/previous 48 hours). Then the method has been applied  
236        to the Red Sea dataset, for the period of July 2017-October 2018. As the period is  
237        short (2 years), we have used the whole period as a test period and Lagrangian



238 catalogue at the same time. For the catalogue period, the 2.5 previous and 2.5 next  
239 days from the target field are removed at each iteration, to avoid overlapping with  
240 the target field.

241

242 To build the Lagrangian catalogue dataset we first generate hourly fields of 25 virtual  
243 particle trajectories advected during 48 hours in the HFR velocity field using a  
244 regular grid of initial positions ( $N^{\circ}= 25$ , Blue dots of Figure 3) inside the HFR gap-  
245 filled OMA current fields domain. Lagrangian module included in the HFR-Progs  
246 MATLAB package was used to compute the trajectories (previously employed to  
247 generate the OMA fields). We follow the same procedure for the test period. For  
248 each hour of the test period, the method searches the most similar Lagrangian  
249 patterns in the Lagrangian catalogue dataset. This process is done in two steps. First,  
250 we look for potential analogues with a similar main drift. To do that we compute and  
251 compare the position of the centroid of the 25 particles during their 48-h trajectories  
252 of the potential analogue with respect to the position of the centroid for the target  
253 field and discard analogues whose center of gravity is at a distance  $> \delta_{cg}$   
254 ( $\delta_{gc}=10\text{km}$  in both HFR systems) from the center of gravity of the final positions  
255 of the target field. The value of the  $\delta_{cg}$  needs to be small enough to minimize  
256 computational time but sufficiently large to as to not lose potential analogues. We  
257 explored different values of this distance threshold and we found that  $\delta_{gc}=10\text{km}$   
258 produces a good compromise between computational cost and number of potential  
259 analogues in both cases. Continuing the selection of the analogue process, in a  
260 second step we compute the Lagrangian errors ( $\mathcal{E}$ ) between the trajectories of the  
261 target field and the fields of the Lagrangian catalogue, defined as:

262

$$263 \quad \mathcal{E} = \Sigma ((\delta_{6h})^2 + (\delta_{12h})^2 + (\delta_{24h})^2 + (\delta_{36h})^2 + (\delta_{48h})^2) \quad \text{Eq. (1)}$$

264



265 where:

- 266 •  $\delta_t$  is the mean separation distance at time  $t$  between the trajectories  
267 belonging to the target field and Lagrangian catalogue field ( $t=6, 12, 24, 36$   
268 or 48 hours in the last 48 hours)
- 269 •  $[\mathcal{E}]=\text{km}^2$

270 Including several hours (6, 12, 24, 36 and 24 hours) to compute the  $\mathcal{E}$  above, resulted  
271 in better estimation values than just considering the separation distance at 48 hours.  
272

273 Finally, the Lagrangian catalogue's field with the lowest error ( $\mathcal{E}$ ) -in terms of  
274 Lagrangian distances- in comparison with the target field is selected as the best  
275 analogue ( $\mathcal{E}_{\text{ANL}} = \min(\mathcal{E})$ ) and the following 48 hours of velocity fields from that  
276 analogue provide the forecasted currents for the target period (hereinafter "L-STP  
277 fields"). Figure 2 shows an example of the values of the errors,  $\mathcal{E}$ , through the  
278 Lagrangian catalogue for a specific case.

279

280 Figure 3 provides an example of the selected analogue (Figure 3b) and  
281 corresponding L-STP fields (Figure 3d) for a given target field (Figure 3a) and the  
282 'realized' trajectories for 48 hours after the target field (Figure 3c). The associated  
283 temporal series of errors for the target field and the potential analogues in the  
284 Lagrangian catalogue are shown in Figure 2, where the minimum error for the  
285 selected analogue ( $\mathcal{E}_{\text{ANL}}$ ) is marked in red dot (corresponding to the error between  
286 the trajectories of the L-STP Figure 3d and the realized trajectories for the forecast  
287 period –Figure 3c).

288

289 To assess the performance of the methodology, we have computed forecasted  
290 trajectories based on persistence of currents (hereinafter 'persistent fields'). To  
291 obtain simulated trajectories using persistence currents, the velocity field of target



292 field at  $t=t_f$  are kept constant and particles are advected during 48 hours using the  
293 constant velocity field:  $v(x,y,t_f+t_i) = v(x,y,t_f)$  where  $t_i = [t_f, t_f+48h]$ . The mean drift  
294 of the realized forecasted trajectories is also computed for each simulation period  
295 (the mean drift is considered as the average of the distances moved by each particle  
296 during 48 hours).

297

298 The Lagrangian errors between the realized trajectories and the STP/Persistent  
299 currents have also been defined and calculated as follows:

300

$$301 \quad \epsilon_{STP} = \sum ((\delta_{-6h})^2 + (\delta_{-12h})^2 + (\delta_{-24h})^2 + (\delta_{-36h})^2 + (\delta_{-48h})^2) \quad \text{Eq. (2)}$$

302

303 where  $\delta_t$  is the mean separation distance between realized field's and STP field  
304 trajectories for  $t = t-48 : t-1$  (last 48 hours)

305

$$306 \quad \epsilon_{PRS} = \sum ((\delta_{-6h})^2 + (\delta_{-12h})^2 + (\delta_{-24h})^2 + (\delta_{-36h})^2 + (\delta_{-48h})^2) \quad \text{Eq. (3)}$$

307

308 where  $\delta_t$  is the mean separation distance between realized field's and Persistent  
309 field trajectories for  $t = t-48 : t-1$  (last 48 hours)

310

311

312 The time series and spatial distribution of the errors of the L-STP ( $\epsilon_{STP}$ ) and  
313 persistence fields ( $\epsilon_{PRS}$ ) have been analyzed for both study areas. Finally,  $\epsilon_{STP}$  and  
314  $\epsilon_{PRS}$  time series have also been calculated and compared to the time series of the  
315  $\epsilon_{ANL}$ , in order to evaluate if the  $\epsilon_{ANL}$  can be used as an indicator of the expected skill  
316 of the L-STP with respect to the persistence.

317



### 318 3. RESULTS

319 The performance assessment results for the BoB HFR system are described in  
320 section 3.1 and the temporal and spatial forecast for both study areas are  
321 demonstrated in section 3.2.

322

#### 323 *3.1 Assessment of the L-STP skills*

324 As described in the methodology, for each hourly time step in the data, the best  
325 analogue for that time step was found (the one with  $\epsilon_{ANL} = \min(\epsilon)$ ). Figure 4 shows  
326 the  $\epsilon_{ANL}$  through year 2015, together with the  $\epsilon_{STP}$  and  $\epsilon_{PRS}$ . The mean value of the  
327  $\epsilon_{PRS}$  is 73% higher than the  $\epsilon_{STP}$ . Black dots over the timeline in Figure 4 show the  
328 times when  $\epsilon_{STP}$  is lower than the  $\epsilon_{PRS}$ , which occurs 75.41% of the time. Focusing  
329 on the times when the  $\epsilon_{PRS}$  is lower than the  $\epsilon_{STP}$  (black dots of the timeline in Figure  
330 4), it can be seen that they mostly occur during winter months. Previous works in  
331 this area have shown that there are high persistent currents during winter months  
332 (Solabarrieta et al., 2014), which is reflected in these results.

333

334 The correlation between  $\epsilon_{ANL}$  and  $\epsilon_{STP}$  is 0.46 while correlation between  $\epsilon_{ANL}$  and  
335  $\epsilon_{PRS}$  is 0.05, for the whole test year (2015) (Figure 4).

336

337 The hourly values of  $\epsilon_{STP}$  (red) and  $\epsilon_{PRS}$  (blue) have been plotted against their  
338 corresponding hourly  $\epsilon_{ANL}$  values for the test year, ordered from minimum to  
339 maximum along the x-axis in Figure 5. We observe that when  $\epsilon_{ANL}$  is low (less than  
340  $853 \text{ km}^2$  for this data set),  $\epsilon_{STP}$  is less than  $\epsilon_{PRS}$ . However, as  $\epsilon_{ANL}$  increases,  $\epsilon_{STP}$  and  
341  $\epsilon_{PRS}$  converge until an inflection point beyond which  $\epsilon_{STP}$  is slightly greater than  $\epsilon_{PRS}$ .  
342 For the SE BoB experiment, the inflection point occurs at  $\epsilon_{ANL} = 853 \text{ km}^2$  and 88%  
343 of cumulative  $\epsilon_{ANL}$ . Results from the Red Sea HFR system indicatses a similar



344 pattern (not shown), when the inflection point occurs at  $\epsilon_{ANL} = 821 \text{ km}^2$  and at 86.4%  
345 of cumulative  $\epsilon_{ANL}$ .

346

347 Further analysis has elucidated the time periods that largely contribute to the errors,  
348 compared to persistence.  $\epsilon_{ANL}$  has been plotted together with the mean separation  
349 distances of the trajectories using STP and persistent currents (hereinafter  $STP_{dist}$   
350 and  $PRS_{dist}$ ), after 6, 12, 24, 36 and 48 hours for each target field (Figure 6). The red  
351 line represents the  $STP_{dist}$  and the blue line represents the  $PRS_{dist}$  for each simulated  
352 scenario (6, 12, 24, 36 or 48 hours). The values of the correlation coefficient ( $R^2$ )  
353 between the  $\epsilon_{ANL}$  and  $STP_{dist}$  and between  $\epsilon_{ANL}$  and  $PRS_{dist}$  after 6, 12, 24, 36 and 48  
354 hours are summarized in Table 2. Values of  $R^2$  for  $PRS_{dist}$  vary between 0.01 and  
355 0.11, while correlations for  $STP_{dist}$  are higher, varying between 0.19 and 0.56,  
356 especially after 12 hours. The behavior of the Red Sea HFR system figures (not  
357 shown) is similar to the BoB HFR system.

358

### 359 *3.2 L-STP performances in the selected study areas*

360 Mean separation distances between realized and forecasted trajectories after  
361 different periods of integration times have been computed for both systems, for the  
362 best functioning analogs, i.e., before the inflection point of  $\epsilon_{STP} > \epsilon_{PRS}$  (Figure 5), in  
363 order to evaluate the temporal forecast capabilities of the methodology. Only  
364 analogues with  $\epsilon_{ANL} < 853 \text{ km}^2$  (BoB system) have been used to generate this  
365 analysis, as those are the periods when the methodology produces good results.  
366 Separation distances computed for the whole test year 2015, are shown in Figure 7,  
367 for the BoB HFR observations.

368



369 The separation distances between the measured trajectories and predicted persistent  
370 and STP trajectories, have similar values during the first 6 hours (4km) of the  
371 forecast period. But after 6 hours, the separation distance for the forecast based on  
372 persistent currents increases faster than using STP. At 24 hours, the separation  
373 distance is 11 km for persistence forecasts and 8km for STP forecasts. The values  
374 are 12 and 18km, respectively, after 48 hours of simulation. The mean drift values  
375 of the ‘realized’ trajectories show that the mean drift is similar to the STP separation  
376 distances, during the 48 hours.

377

378 Temporal mean separation distances between realized and forecasted trajectories for  
379 the Central Red Sea HFR System, computed for the whole test time (July 2017-  
380 October 2018), are shown in Figure 8. Only winner analogues with  $\varepsilon_{ANL}$  less than  
381 inflection point, i.e.,  $\varepsilon_{ANL} < 821\text{km}^2$ , have been used to generate this analysis. The  
382 separation distances for the STP forecasts are higher than those forecasts with  
383 persistent currents during the first 15 hours. After 15 hours, quality of forecasts  
384 reversed where STP produced better results than persistence.

385

386 Spatial distribution of the difference between STPdist and PRSdist at 6, 12, 24 and  
387 48 hours, for the BoB and the Red Sea HFR systems, are shown in Figure 9 and  
388 Figure 10.

389 For the BoB HFR system, the differences are not appreciated during the first 6 hours.  
390 But after 12 hours of simulation, the advantage of the STP is clear in most of the  
391 study area, especially outside the continental shelf slope where persistent currents  
392 dominate the circulation. The separation values increase up to 10km after 48hours  
393 of simulation.

394



395 For the Red Sea HFR system, the significant differences between STP and  
396 Persistence start after 24 hours of simulation, and continue until 48 hours.



397 **4. DISCUSSION**

398 In this work, a new methodology to forecast HFR currents has been described and  
399 the skill of the proposed STP methodology is analyzed. Different analyses were  
400 performed in order to check the spatial and temporal capabilities of the proposed  
401 methodology.

402

403 The methodology is based on the search of analogues in a trajectory space using a  
404 previously generated trajectory field catalogue. The analogue finding was first  
405 applied to surface velocity fields rather than in the trajectory space of the BoB HFR  
406 System, but the results did not improve the previously published STP results for the  
407 study area. Analogue finding method was later applied to Lagrangian trajectory  
408 fields, advected using the HFR velocity fields. The values of the  $STP_{dist}$ , compared  
409 to previous works showed that analogue finding produces more accurate predictions  
410 if it is applied to Lagrangian trajectories than does the application to surface current  
411 velocities. This shows the ability of the Lagrangian approach to capture key  
412 dynamical features needed to accurately predict the proper dynamical conditions.

413

414 Correlation values between  $\epsilon_{ANL}$  and  $PRS_{dist}$  vary between 0.01 and 0.11, showing  
415 no significant correlation (Table 2). The values using  $STP_{dist}$  are higher, varying  
416 between 0.19 and 0.56 (Table 2 and Figure 6). During the test period for the BoB  
417 HFR system,  $\epsilon_{STP}$  is lower than the  $\epsilon_{PRS}$  about 88% of the time (Figure 5). The 12%  
418 of the time when the persistence results are better (black dots over the timeline of  
419 Figure 4) occurs mostly during wintertime when  $\epsilon_{ANL}$  is larger. As stated in previous  
420 work, that the circulation over the BoB area is dominated by a stable, persistent  
421 current field during winter (Solabarrieta et al., 2014) which is reflected by these



422 results where persistence has good or even slightly better forecasting skill during the  
423 first and only the first, forecast hours than the proposed methodology.

424

425 Figure 6 shows that after 12 hours of simulation, the STP forecast provides a better  
426 prediction than the prediction from Persistence for more than 80% of the cases  
427 (reaching more than 90% of the cases for 36 and 48 hours of simulation). The  
428 minimum  $\epsilon_{ANL}$  value for the  $STP_{dist}$  and  $PRS_{dist}$  cross point is  $714\text{km}^2$ . Figure 5, for  
429 the total  $\epsilon_{ANL}$  shows the same behavior being  $815\text{km}^2$  the transition analogue error  
430 value between STP and Persistence.

431

432 The results suggest that the  $\epsilon_{ANL}$  can be considered as a real-time skill-score metric  
433 for the L-STP. Both BoB and the central Red Sea show a similar behavior; although  
434 the  $\epsilon_{ANL}$  values are different, the accumulative % of the transition point is similar in  
435 both cases.

436

437 For the BoB HFR System, temporal  $STP_{dist}$  show values of 3.5km, 5.5km and 8km,  
438 after 6, 12, and 24 hours respectively. The  $STP_{dist}$  values are similar to the  $PRS_{dist}$   
439 values during the first 6 hours of simulation but  $STP_{dist}$  are lower after that, with 3km  
440 and 5.5km of difference between them, after 24 and 48 hours of simulation,  
441 respectively (Figure 4).

442

443 The  $STP_{dist}$  values for the BoB HFR system are similar to the ones obtained by  
444 Solabarrieta et al., 2016, for the whole year but  $STP_{dist}$  are better for summer months,  
445 for the same study area. They used the linear autoregressive model, described in  
446 Frolov et al., 2012, to forecast HFR current fields and the errors using that approach  
447 were 2.9 and 7.9km after 6 and 24 hours. Although the results obtained in this work  
448 improve only during certain periods the forecast presented in Solabarrieta et al. 2016,



449 the presented methodology has three advantages over the previous method: it is  
450 easily run in real time; it does not require a continuous training period; and it is able  
451 to discriminate the times when the usage of the persistence is applicable. On the  
452 negative side, it requires the generation of a catalogue of past trajectories as the  
453 search space for analogues.

454

455 The values of the  $STP_{dist}$  for the Red Sea HFR system follow a similar pattern to the  
456 BoB results, with higher separation distances. This may be related to the limited time  
457 span of the available dataset, as a better closest analogue may be found in a longer  
458 dataset.

459

460 The spatial comparison of the  $STP_{dist}$  and  $PRS_{dist}$  for the BoB HFR system (Figure  
461 9), shows that the STP has better results in all of the study area after 12 hours of  
462 simulations. The advantage of the methodology increases with time, showing 10km  
463 of improvement relative to persistence. For the spatial distribution, after 12 hours,  
464 the least improvement of the L-STP methodology relative to Persistence occurred  
465 over the slope. This is explained by existence of persistent seasonal Iberian Poleward  
466 Current that flows along the continental slope toward the east along the Spanish  
467 coast and northward along the French coast (Solabarrieta et al. 2014).

468 The results for the Red Sea HFR system are similar but the benefit of the L-STP  
469 methodology appears after 12 hours of simulation. Spatially, the improvement is  
470 again lower where persistent currents occur, as it is the case of the Eastern Boundary  
471 Current that flows northward following the eastern Red Sea Coastline in the study  
472 area (Bower and Farrah, 2015; Sofianos and Johns, 2003; Zarokanellos et al., 2017).

473 The dominance of the persistent currents is clearly evident in the lower values of the  
474 difference between the STP forecasts and the Persistence forecasts as shown in  
475 Figure 10 and in comparison with Figure 9.



476

477 We have compared the capabilities of the L-STP forecast against the forecast based  
478 on the persistency of currents. The L-STP method requires long training periods but  
479 performs better during non-persistent periods. Previous efforts to forecast surface  
480 currents from HFR data have shown similar results compared with the methodology  
481 presented in this paper. However, the advantage of the L-STP method is that it can  
482 be used anytime, with short datasets of around 2-3 years, even if that data set contains  
483 temporal gaps.

484

485 The HFR Progs MATLAB package ([https://](https://cencalarchive.org/~cocmpmb/COCMPwiki)  
486 [cencalarchive.org/~cocmpmb/COCMPwiki](https://cencalarchive.org/~cocmpmb/COCMPwiki)) has been used to generate total currents  
487 from radial files to fill the spatial gaps of the surface current field using the OMA  
488 method, and to generate Lagrangian trajectories. This methodology could be easily  
489 included in this package so the final users could get forecast currents, in the same  
490 time that they generate total currents.

491



492 **5. CONCLUSION**

493 A methodology to forecast currents in real-time has been proposed. This  
494 methodology provides accurate forecast of sea surface currents and its capability has  
495 been tested in terms of spatial and temporal distributions. The good functioning and  
496 confidence of this methodology has been demonstrated in the previous sections and  
497 also, its capability to be applied in real time. The methodology has been applied to  
498 2 distinct coastal regions to evaluate its capabilities in different conditions. Although  
499 further analysis using data from more areas is required to generalize the  
500 methodology, these initial results indicate that it works similarly in the 2 different  
501 analyzed study areas, suggesting that it can be generalized.

502

503 A primary advantage of the proposed methodology compared with previous  
504 approaches is that it is easily implemented in real time.

505

506 Relationships between  $\epsilon_{ANL}$  and  $\epsilon_{STP}/\epsilon_{PRS}$  suggest that the  $\epsilon_{ANL}$  can be considered as  
507 a well-functioning indicator of the method's performance. Taking in consideration  
508 all the analyses done in this work, we propose to use STP currents for trajectory or  
509 velocity field predictions from 12 hours forward, if the  $\epsilon_{ANL}$  value is lower than  
510 80% of the cumulative  $\epsilon_{ANL}$  (714 km<sup>2</sup> in the case of the BoB HFR system). If  $\epsilon_{ANL}$  is  
511 higher, or the forecast is just for the next 6 hours, the use of the last available hour,  
512 as persistent current is suggested. We also suggest that the  $\epsilon_{ANL}$  value and forecast  
513 transition time need to be carefully evaluated for each study region. This, of course,  
514 infers that a minimum data set is required before the STP method can began to be  
515 applied.

516



517 Further analysis of analogue finding approaches is required to improve the observed  
518 results, especially during periods when currents are persistent. The usage of longer  
519 dataset as a training period may help on this as well. The next step would be to test  
520 the methodology for additional periods and other regions, and to evaluate its  
521 functionality in an operational mode.

522

523 The analysis to find the minimum training period for each system should be analyzed  
524 deeper in future works, as the application of the STP forecast to the Red Sea HFR  
525 system should improve as the observational time period increases. The minimum  
526 training period will be directly related to the variability of the local dynamics and  
527 those should be considered during the analysis.

528

529 In case of an oil spill, the proposed methodology offers an accurate forecast of the  
530 surface currents for up to 48 hours in advance. But it is important to note that for the  
531 oil spill prediction, the influence of the wind and waves in combination with the  
532 surface currents also needs to be considered.



533 **DATA AVAILABILITY**

534

535 The Red Sea HF Radar data can be requested through:

- 536 • <https://lthdatalib.kaust.edu.sa>

537

538 Historical and NRT Bay of Biscay HF Radar data can be requested through:

- 539 • Euskoos portal: [https://www.euskoos.eus/en/data/basque-ocean-](https://www.euskoos.eus/en/data/basque-ocean-meteorological-network/high-frequency-coastal-radars/)  
540 [meteorological-network/high-frequency-coastal-radars/](https://www.euskoos.eus/en/data/basque-ocean-meteorological-network/high-frequency-coastal-radars/)

- 541 • Emodnet Physics -

542 <http://www.emodnetphysics.eu/Map/platinfo/piradar.aspx?platformid=10>  
543 [273](http://www.emodnetphysics.eu/Map/platinfo/piradar.aspx?platformid=10)

- 544 • CMEMS Instac - [http://marine.copernicus.eu/services-portfolio/access-to-](http://marine.copernicus.eu/services-portfolio/access-to-products/?option=com_csw&view=details&product_id=INSITU_GLO_UV_N)  
545 [products/?option=com\\_csw&view=details&product\\_id=INSITU\\_GLO\\_UV\\_N](http://marine.copernicus.eu/services-portfolio/access-to-products/?option=com_csw&view=details&product_id=INSITU_GLO_UV_N)  
546 [RT\\_OBSERVATIONS\\_013\\_048](http://marine.copernicus.eu/services-portfolio/access-to-products/?option=com_csw&view=details&product_id=INSITU_GLO_UV_N)

547



548 **AUTHORS CONTRIBUTION**

- 549       • Lohitzune Solabarrieta: She has worked on the set up of the methodology,  
550       data analysis, manuscript writing and final submission.
- 551       • Ismael Hernandez-Carrasco: He has worked on the set up of the  
552       methodology and the manuscript writing.
- 553       • Anna Rubio: She has worked on the set up of the methodology, data analysis,  
554       and manuscript writing.
- 555       • Alejandro Orfila: He has worked on the configuration of the methodology,  
556       data analysis and the manuscript writing.
- 557       • Michael Campbell: He has worked on the configuration of the methodology,  
558       especially in the pre-configuration that led us to rule out other data  
559       prediction methodologies. He has also contributed on the manuscript  
560       writing.
- 561       • Ganix Esnaola: He has worked on the configuration of the methodology,  
562       especially in the pre-configuration that moved us to the usage of analogues  
563       on this paper. He has also contributed on the manuscript writing.
- 564       • Julien Mader: He has contributed on the writing of the manuscript.
- 565       • Burton H. Jones: He has contributed on the writing of the manuscript

566

567

568



569 **COMPETING INTERESTS**

570

571 The authors declare that we have no conflict of interest

572



573 **ACKNOWLEDGEMENTS**

574 This work was funded by a Saudi Aramco-KAUST Center for Marine  
575 Environmental Observation (SAKMEO) Postdoc fellowship to Lohitzune  
576 Solabarrieta, and from the Integrated Ocean Processes (IOP) Group in KAUST. We  
577 acknowledge the support of the LIFE-LEMA project (LIFE15 ENV/ES/000252), the  
578 European Union's Horizon 2020 research and innovation program under grant  
579 agreement No. 654410 (JERICO-NEXT Project), the Directorate of Emergency  
580 Attention and Meteorology of the Basque Government, the MINECO/FEDER  
581 Projects MUSA and MOCCA (CTM2015-66225-C2-2-P; 256RTI2018-093941-B-  
582 C31). and the Department of Environment, Regional Planning, Agriculture and  
583 Fisheries of the Basque Government (Marco Program). This work was partially  
584 performed while A. Orfila was a visiting scientist at the Earth, Environmental and  
585 Planetary Sciences Department at Brown University through a Ministerio de  
586 Ciencia, Innovación y Universidades fellowship (PRX18/00218). Ismael  
587 Hernandez-Carrasco acknowledges the Vicenç Mut contract funded by the Balearic  
588 Island Govern and the European Social Fund (ESF) Operational Programme.

589

590 The HF radar-processing toolbox HFR\_Progs use to produce OMA was provided by  
591 D. Kaplan and M. Cook, Naval Postgraduate School, Monterey, CA, USA.

592

593

594

595

596

597



598 **REFERENCES**

- 599 Abascal, A. J., Castanedo, S., Medina, R., Losada, I. J., Álvarez-Fanjul, E.:  
600 Application of HF radar currents to oil spill modelling. *Mar. Pollut. Bull.* 58  
601 (2), 238–248, 2009
- 602 Abascal A. J., Sanchez, J., Chiri, H., Ferrer, M. I., Cárdenas, M., Gallego, A.,  
603 Castanedo, S., Medina, R., Alonso-Martirena, A., Berx, B., Turrell, W. R.,  
604 Hughes, S. L.: Operational oil spill trajectory modelling using HF radar  
605 currents: A northwest European continental shelf case study. *Marine Pollution*  
606 *Bulletin*, Volume 119, Issue 1, Pages 336-350, ISSN 0025-326X,  
607 <https://doi.org/10.1016/j.marpolbul.2017.04.010>, 2017.
- 608 Abualnaja, Y., Papadopoulos, V. P., Josey, S. A., Hoteit, I., Kontoyiannis, H., and  
609 Raitsos, D. E.: Impacts of climate modes on air–sea heat exchange in the Red  
610 Sea, *J. Clim.*, 28, 2665–2681, doi:10.1175/JCLI-D-14-00379.1, 2015.
- 611 Barrick, D. E.: Extraction of wave parameters from measured HF radar sea-echo  
612 Doppler spectra. *Radio Sci.*, 12, 415–424, doi:10.1029/RS012i003p00415,  
613 1977.
- 614 Barrick D.E., Fernandez, V., Ferrer, M.I., Whelan, C., and Breivik, Ø.: “A short-  
615 term predictive system for surface currents from a rapidly deployed coastal  
616 HF-Radar network,” *Ocean Dyn.*, vol. 62, no. 5, pp. 725–740, 2012.
- 617 Barth, A., Alvera-Azcárate, A., Beckers, JM., Staneva J., Stanev E.V., and Schulz-  
618 Stellenfleh J.: Correcting surface winds by assimilating high-frequency radar  
619 surface currents in the German Bight. *Ocean Dynamics*, 2011, vol 61: 599.  
620 <https://doi.org/10.1007/s10236-010-0369-0>, 2011.
- 621 Bellomo, L., Griffa, A., Cosoli, S., Falco, P., Gerin, R., Iermano, I., Kalampokis, A.,  
622 Kokkini, Z., Lana, A., Magaldi, M.G., Mamoutos, I., Mantovani, C.,  
623 Marmain, J., Potiris, E., Sayol, J.M., Barbin, Y., Berta, M., Borghini, M.,  
624 Bussani, A., Corgnati, L., Dagneaux, Q., Gaggelli, J., Guterman, P.,



- 625           Mallarino, D., Mazzoldi, A., Molcard, A., Orfila, A., Poulain, P. M., Quentin,  
626           C., Tintoré, J., Uttieri, M., Vetrano, A, Zambianchi, E. and Zervakis, V.:  
627           Toward an integrated HF radar network in the Mediterranean Sea to improve  
628           search and rescue and oil spill response: the TOSCA project experience.  
629           Toward an integrated HF radar network in the Mediterranean Sea to improve  
630           search and rescue and oil spill response: the TOSCA project experience,  
631           Journal of Operational Oceanography, 8:2, 95-107, DOI:  
632           10.1080/1755876X.2015.1087184, 2015.
- 633   Bower, A. S., and Farrar, J. T.: Air–sea interaction and horizontal circulation in the  
634           Red Sea. In N. M. A. Rasul & I. C. F. Stewart, (Eds.), The Red Sea, Springer  
635           Earth System Sciences (pp. 329–342). Berlin, Germany: Springer.  
636           [https://doi.org/10.1007/978-3-662-45201-1\\_19](https://doi.org/10.1007/978-3-662-45201-1_19), 2015.
- 637   Breivik, Ø, and Saetra, Ø.: Real time assimilation of HF radar currents into a coastal  
638           ocean model. Journal of Marine Systems, Volume 28, Issues 3–4, April 2001,  
639           Pages 161-182. [https://doi.org/10.1016/S0924-7963\(01\)00002-1](https://doi.org/10.1016/S0924-7963(01)00002-1), 2001.
- 640   Chao, Y., Li Z., Farrara, K., McWilliams, J.C., Bellingham, J., Capet, X., Chavez,  
641           F., Choi, J., Davis, R., Doyle, J., Fratantoni, D. M., Li P., Marchesiello, P.,  
642           Moline, M.A., Paduan, J., Ramp, S.: Development, implementation and  
643           evaluation of a data-assimilative ocean forecasting system off the central  
644           California coast. Deep Sea Research, Vol. 56, Issues 3-5, pp 100-126.  
645           <https://doi.org/10.1016/j.dsr2.2008.08.011>, 2009.
- 646   Crombie, D. D.: Doppler Spectrum of Sea Echo at 13.56-Mc/s’, Nature 175, 681-682,  
647           1955.
- 648   Emery, B. M., Washburn L., and Harlan, J. A.: Evaluating radial current  
649           measurements from CODAR high-frequency radars with moored current  
650           meters. J. Atmos. Oceanic Tech- nol., 21, 1259–1271, doi:10.1175/1520-  
651           0426(2004)021,1259: ERCMFC.2.0.CO;2, 2004.



- 652 Esnaola, G., Sáenz, J., Zorita, E., Fontán, A., Valencia, V., and Lazure, P.: Daily  
653 scale wintertime sea surface temperature and IPC-Navidad variability in the  
654 southern Bay of Biscay from 1981 to 2010, *Ocean Sci.*, 9, 655–679,  
655 <https://doi.org/10.5194/os-9-655-2013>, 2013.
- 656 Fernández-Ferrero, A., Sáenz, J., Ibarra-Berastegi, G., Fernández, J.: Evaluation of  
657 statistical downscaling in short range precipitation forecast. *Atmos. Res.* 94,  
658 448–461, 2009.
- 659 Fernández-Ferrero, A., Sáenz, J., Ibarra-Berastegi, G.: Comparison of the  
660 performance of different Analog-Based Bayesian probabilistic precipitation  
661 forecasts over Bilbao, Spain. *Mon. Weather Rev.* 38, 3107–3119, 2010.
- 662 Frolov, S., Paduan J., Cook M., and Bellingham J.: Improved statistical prediction  
663 of surface currents based on historic HF- radar observations. *Ocean Dyn.*, 62,  
664 1111–1122, doi:10.1007/s10236-012-0553-5, 2012.
- 665 Hammond, T.M., Pattiaratchi, C.B., Osborne, M.J., Nash, L.A., Collins, M.B.:  
666 Ocean surface current radar (OSCR) vector measurements on the inner  
667 continental shelf. *Continental Shelf Research*. Volume 7, Issue 4, Pages 411-  
668 431. [https://doi.org/10.1016/0278-4343\(87\)90108-7](https://doi.org/10.1016/0278-4343(87)90108-7), 1987.
- 669 Hernández-Carrasco, I., Solabarrieta, L., Rubio, A., Esnaola, G., Reyes, E., and  
670 Orfila, A.: Impact of HF radar current gap-filling methodologies on the  
671 Lagrangian assessment of coastal dynamics, *Ocean Sci.*, 14, 827-847,  
672 <https://doi.org/10.5194/os-14-827-2018>, 2018.
- 673 Hernández-Carrasco, I., Orfila, A., Rossi, V., and Garçon, V.: Effect of small-scale  
674 transport processes on phytoplankton distribution in coastal seas, *Scientific*  
675 *Reports*, 8:8613, <https://doi.org/10.1038/s41598-018-26857-9>, 2018b.
- 676 Ibarra-Berastegi, G., Saenz, J., Ezcurra, A., Ezcurra, A., Elias, A., Diaz Argandona,  
677 J., Errasti, I.: Downscaling of surface moisture flux and precipitation in the  
678 Ebro Valley (Spain) using analogues and analogues followed by random



- 679 forests and multiple linear regression. *Hydrol. Earth Syst. Sci.* 15 (6), 1895–  
680 1907, 2011.
- 681 Jianping H., Yuhong Y., Shaowu W and Jifen C.: An analogue-dynamical long-  
682 range numerical weather prediction system incorporating historical evolution.  
683 *Q. J. R. Meteorol. Soc.*, 119, pp.547-565, 1993.
- 684 Kaplan, D. M. and Lekien, F.: Spatial interpolation and filtering of surface current  
685 data based on open-boundary modal analysis, *Journal of Geophysical*  
686 *Research: Oceans*, 112, <https://doi.org/10.1029/2006JC003984>, c12007,  
687 2007.
- 688 Kohut, J.T., Glenn, S.M.: Improving HF radar surface current measurements with  
689 measured antenna beam patterns. *J. Atmos. Oceanic Technol.* 20 (9), 1303–  
690 1316, 2003.
- 691 Lana, A., Marmain, J., Fernández, V., Tintoré, J., Orfila A.: Wind influence on  
692 surface current variability in the Ibiza Channel from HF Radar. *Ocean*  
693 *Dynamics*, 66: 483. <https://doi.org/10.1007/s10236-016-0929-z>, 2016
- 694 Langodan S., Cavaleri L., Vishwanadhapalli Y., Pomaro A., Bertotti L., Hoteit I.:  
695 Climatology of the Red Sea - Part 1: the wind. *Int. J. Climatol.* 37: 4509–4517.  
696 DOI: 10.1002/joc.5103, 2017.
- 697 Liu Y., Weisberg, R.H., and Merz, C.R.: Assessment of CODAR SeaSonde and  
698 WERA HF Radars in Mapping Surface Currents on the West Florida Shelf.  
699 *Journal of atmospheric and oceanic technology*, Vol 31., pp 1363:1382, 2014.
- 700 Lorenz, E. N.: Atmospheric Predictability as Revealed by Naturally Occurring  
701 Analogues. *Journal of Atmospheric Sciences*, Volume 29, pp 636-646, 1969.
- 702 Martin, M.L., Valero, F., Pascual, A., Sanz, J., and Frias, L.: Analysis of wind power  
703 productions by means of an analog model. *Atmos. Res.* 143, 238–249, 2014.



- 704 Oke, P. R., Allen, J. S., Miller, R. N., Egbert, G. D., and Kosro P. M.: Assimilation  
705 of surface velocity data into a primitive equation coastal ocean model, J.  
706 Geophys. Res., 107, 3122, doi:10.1029/2000JC000511, 2002.
- 707 Orfila A., Molcard, A., Sayol, J.M., Marmain, J., Bellomo, L., Quentin, C., and  
708 Barbin, Y.: Empirical Forecasting of HF-Radar Velocity Using Genetic  
709 Algorithms IEEE Transactions on Geoscience and Remote Sensing, Vol. 53,  
710 No. 5, 2015.
- 711 Ohlmann, C., White, P., Washburn, L., Emery, B., Terrill, E., Otero, M.:  
712 Interpretation of coastal HF radar–derived surface currents with high-  
713 resolution drifter data. J. Atmos. Oceanic Technol. 24 (4), 666–680, 2007.
- 714 Paduan, J.D., and Rosenfeld, L.K.: Remotely sensed surface currents in Monterey  
715 Bay from shore-based HF radar (coastal ocean dynamics application radar. J.  
716 Geophys. Res. 101 (C9), 20669–20686, 1996.
- 717 Paduan, J.D., and Shulman, I.: HF radar data assimilation in the Monterey Bay area.  
718 J. Geophys Res. 109:C07S09, 2004.
- 719 Paduan, J.D., Kim, K.C., Cook, M. S., and Chavez, F.P.: Calibration and Validation  
720 of Direction-Finding High-Frequency Radar Ocean Surface Current  
721 Observations. IEEE Journal of oceanic engineering, Vol. 31, No. 4, 2006.
- 722 Paduan, J.D., and Washburn, L.: High-Frequency Radar Observations of Ocean  
723 Surface Currents. Annual Rev. Marine. Sci. 2013.5:115-136, 2013.
- 724 Prince, K., X. and Goswami, B., N.: An Analog Method for Real-Time Forecasting  
725 of Summer Monsoon Subseasonal Variability. Monthly weather review, Vol  
726 135, pp: 4149-4160. <https://doi.org/10.1175/2007MWR1854.1>, 2007.
- 727 Ren L., Miaro, J., Li Y., Luo, X., Li J. and Hartnett, M.: Estimation of Coastal  
728 Currents Using a Soft Computing Method: A Case Study in Galway Bay,  
729 Ireland. Mar. Sci. Eng., 7(5), 157; <https://doi.org/10.3390/jmse7050157>, 2019



- 730 Roarty, H., Cook, T., Hazard, L., George, D., Harlan, J., Cosoli, S., Wyatt, L.,  
731 Alvarez Fanjul, E., Terrill, E., Otero, M., Largier, J., Glenn, S., Ebuchi, N.,  
732 Whitehouse, B., Bartlett, K., Mader, J., Rubio, A., Corgnati, L., Mantovani,  
733 C., Griffa, A., Reyes, E., Lorente, P., Flores-Vidal, X., Saavedra-Matta, K.J.,  
734 Rogowski, P., Prukpitikul, S., Lee, S.H., Lai, J.W., Guerin, C.A., Sanchez, J.,  
735 Hansen, B. and Grilli, S.: The Global High Frequency Radar Network. *Front.*  
736 *Mar. Sci.* 6:164. doi: 10.3389/fmars.2019.00164, 2019 (in press).
- 737 Schmidt, R.: Multiple emitter location and signal parameter estimation. *IEEE Trans.*  
738 *Antennas Propag.*, 34, 276–280, doi:10.1109/TAP.1986.1143830, 1986.
- 739 Schott F., Frisch, A.S., Leaman, K., Samuels, G., Popa Fotino, I.: High-Frequency  
740 Doppler Radar Measurements of the Florida Current in Summer 1983. *J. Geo.*  
741 *Research*, Vol 90, No C5, pp 9006:9016, 1985.
- 742 Seubert, S., Fernández-Montes, S., Philipp, A., Hertig, E., Jacobeit, J., Vogt, G.,  
743 Paxian, A., Paeth, H.: Mediterranean climate extremes in synoptic  
744 downscaling assessments. *Theor. Appl. Climatol.* 117 (1–2), 257–275, 2014.
- 745 Shao, Q. and Li, M.: An improved statistical analogue downscaling procedure for  
746 seasonal precipitation forecast. *Stoch Environ Res Risk Assess* 27, pp.: 819-  
747 830. <https://doi.org/10.1007/s00477-012-0610-0>, 2013.
- 748 Sofianos, S. S., and Johns, W. E.: An oceanic general circulation model (OGCM)  
749 investigation of the Red Sea circulation: 2. Three- dimensional circulation in  
750 the Red Sea. *Journal of Geophysical Research*, 108(C3), 3066.  
751 <https://doi.org/10.1029/2001jc001185>, 2003.
- 752 Solabarrieta, L., Rubio, A., Castanedo, S., Medina, R., Charria, G., Hernández, C.:  
753 Surface water circulation patterns in the southeastern Bay of Biscay: new  
754 evidences from HF radar data. *Cont Shelf Res* 74:60–76  
755 doi:10.1016/j.csr.2013.11.022, 2014.



- 756 Solabarrieta, L., Rubio, A., Cárdenas, M., Castanedo, S., Esnaola, G., Méndez, F.J.,  
757 Medina, R., and Ferrer, L.: Probabilistic relationships between wind and  
758 surface water circulation patterns in the SE Bay of Biscay. *Ocean Dyn.*, 65,  
759 1289–1303, doi:10.1007/s10236-015-0871-5, 2015.
- 760 Solabarrieta, L., Frolov, S., Cook, M., Paduan, J., Rubio, A., González, M., Mader,  
761 J., and Charria, G.: Skill Assessment of HF Radar-Derived Products for  
762 Lagrangian Simulations in the Bay of Biscay. *J. Atmos. Oceanic Technol.*, 33,  
763 2585–2597, doi: 10.1175/JTECH-D-16-0045.1, 2016.
- 764 Stanev, E.V., Schulz-Stellenfleth, J., Staneva, J., Grayek, S., Seemann, J. and  
765 Petersen, W.: Coastal observing and forecasting system for the German Bight  
766 – estimas of hydrophysical states. *Ocean Sci.*, 7, 569–583, 2011  
767 doi:10.5194/os-7-569-2011, 2011.
- 768 Ullman, D.S., O'Donnell, J., Kohut, J., Fake, T., Allen, A.: Trajectory prediction  
769 using HF radar surface currents: Monte Carlo simulations of prediction  
770 uncertainties. *J. Geophys. Res.* 111 (C12005), 1–14, 2006.
- 771 Vilibić, I., Šepić, J., Mihanović, H., Kalinić, H., Cosoli, S., Janeković, I., Žagar, N.,  
772 Jesenko, B., Tudor, M., Dadić, V. and Ivanković, D.: Self-organizing maps-  
773 based ocean currents forecasting system. *Scientific Reports* 6, 22924, 2016.
- 774 Yao, F., Hoteit, I., Pratt, L. J., Bower, A. S., Zhai, P., Kohl, A., and Gopalakrishnan,  
775 G.: Seasonal overturning circulation in the Red Sea: 1. Model validation and  
776 summer circulation, *J. Geophys. Res. Oceans*, 119, doi:10.1002/  
777 2013JC009004, 2014.
- 778 Yao, F., Hoteit, I., Pratt, L. J., Bower, A. S., Kohl, A., Gopalakrishnan, G., and  
779 Rivas, D.: Seasonal overturning circulation in the Red Sea: 2. Winter  
780 circulation, *J. Geophys. Res. Oceans*, 119, 2263–2289, doi:10.1002/  
781 2013JC009331, 2014.



- 782 Zarokanellos, N. D., Kürten, B., Churchill, J. H., Roder, C., Voolstra, C. R.,  
783 Abualnaja, Y., and Jones, B. H.: Physical mechanisms routing nutrients in the  
784 central Red Sea. *Journal of Geophysical Research: Oceans*, 122.  
785 <https://doi.org/10.1002/2017JC013017>, 2017a.
- 786 Zarokanellos, N. D., Papadopoulos, V. P., Sofianos, S. S., and Jones, B. H.: Physical  
787 and biological characteristics of the winter-summer transition in the Central  
788 Red Sea. *Journal of Geophysical Research: Oceans*, 122, 6355–6370.  
789 <https://doi.org/10.1002/2017JC012882>, 2017b.
- 790 Zhan, P., Subramanian, A. C., Yao, F., and Hoteit, I.: Eddies in the Red Sea: A  
791 statistical and dynamical study, *J. Geophys. Res. Oceans*, 119, 3909–3925,  
792 doi:10.1002/2013JC009563, 2014.
- 793 Zelenke B. C.: An Empirical Statistical Model Relating Winds and Ocean Surface  
794 Currents. Master of Science in Oceanography - Thesis, Oregon State  
795 University, 2005.
- 796 Zorita E, and von Storch H.: The analog method as a simple statistical downscaling  
797 technique: comparison with more complicated methods. *J Climate* 12:2474–  
798 2489, 1999.
- 799



800 **TABLES**

801

802 *Table 1: Characteristics of the previously developed STP works based on HFR data.*

<b>Authors</b>	<b>Approach</b>	<b>Needs continuous training period</b>	<b>Complementary data required?</b>	<b>Region of application</b>	<b>Reliable forecast period</b>
Zelenke 2005	EOF + bilinear regression model	Yes	Wind	Oregon coast	48 hours
Frolov et al. 2012	EOF + linear auto regression model	Yes	Wind and tides (optional)	Monterey Bay, California	48 hours
Barrick et al., 2012	Constant linear trend model applied to OMA modes	Yes	Wind	Finmark, Norway	12 hours
Orfila et al. 2015	EOF+Genetic Algorithm	Yes	No	Toulon, France	48 hours
Solabarrieta et al. 2016	Frolov et al., 2012	Yes	No	Bay of Biscay	48 hours
Vilibić et al., 2016	SOM+neural network +winds	Yes	Wind	Northern Adriatic Sea	72 h
Ren et al., 2019	Random Forest (RF) classification algorithm	No	Tide and Wind	Galway Bay, Ireland	59 h
This paper: L-STP	Analogue finding	No	No	Bay of Biscay and the Central Red Sea	48 h

803



804 *Table 2: Correlation coefficient values between winner  $\epsilon_{ANL}$  and  $STP_{dist}$  and between  $\epsilon_{ANL}$  and*  
 805  *$PRS_{dist}$ , after 6, 12, 24, 36 and 48 hours of simulation.*  
 806

	<b>6 hours</b>	<b>12 hours</b>	<b>24 hours</b>	<b>36 hours</b>	<b>48 hours</b>
<b><math>R^2</math> <math>\epsilon_{ANL} - STP_{dist}</math></b>	0.19	0.37	0.55	0.56	0.54
<b><math>R^2</math> <math>\epsilon_{ANL} - PRS_{dist}</math></b>	0.07	0.11	0.03	0.01	0.04
$\epsilon_{ANL}$ [km <sup>2</sup> ], for the inflection point between $STP_{dist}$ and $PRS_{dist}$	-	714	774	857	1027
% of $\epsilon_{ANL}$ (accumulative) for the previous line	-	81	84	87	95

807

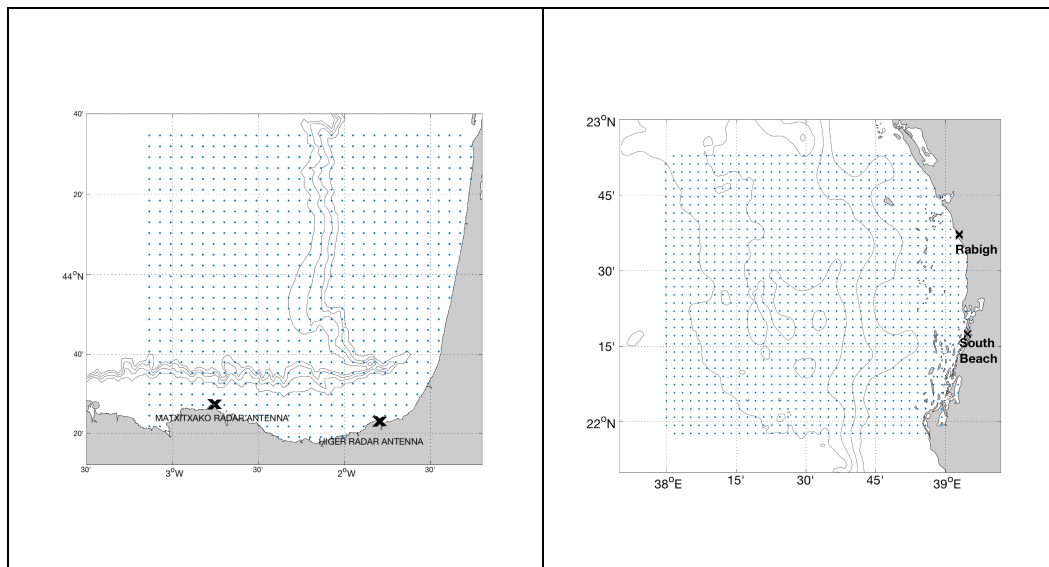


808 **FIGURES**

809

810 *Figure 1: (Left) HFR system of the BoB. (Right) HFR system of the central Red Sea.*  
811 *Blue dots represent the data points and the black cross are the HFR antenna*  
812 *positions*

813



814

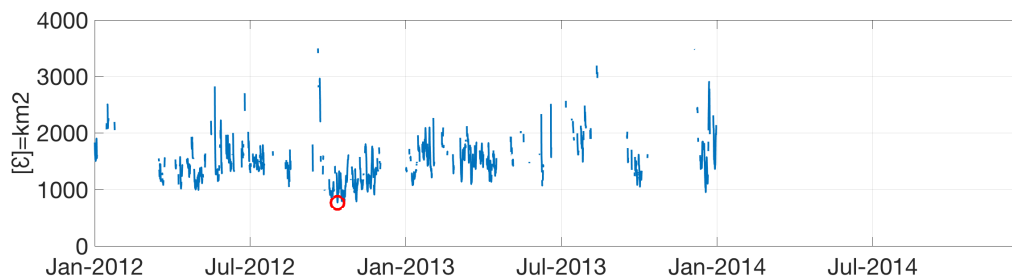
815

816



817 *Figure 2: Example for the test period: 17-Nov-2015 00:00; errors for the whole*  
818 *Lagrangian catalogue fields of the BoB HFR System, restricted to the  $\delta\_cg = 10$  km*  
819 *condition. The red dot indicates the occurrence date and the error of the winner*  
820 *analogue.*

821



822

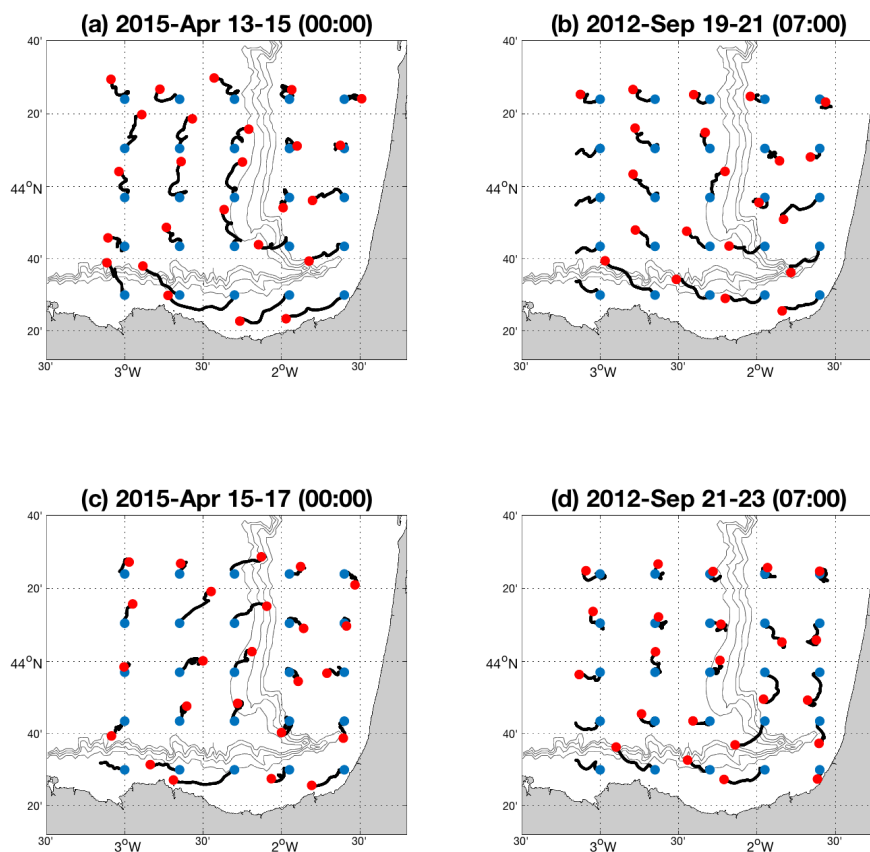
823

824



825 *Figure 3: (1) 15-Apr-2015 00:00 example of the developed methodology applied to*  
826 *the BoB HFR system. (a) The past 48 hours of target field of test period (b) The*  
827 *analogue having the lowest error, (c) The realized trajectories for the forecast*  
828 *period (d) the STP trajectories. The initial positions of the particle trajectories are*  
829 *indicated by the blue dots, and the red dots indicate the position after 48 hours.*

830

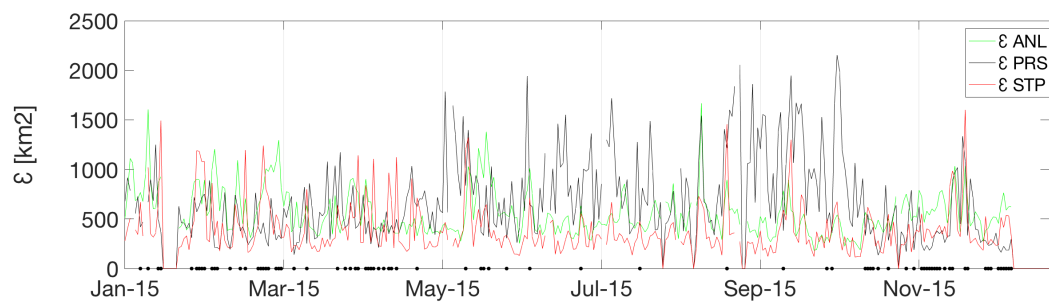


831

832



833 *Figure 4: errors of the hourly winner analogue for 2015 ( $\epsilon_{ANL}$ ), together with the*  
834  *$\epsilon_{STP}$  and  $\epsilon_{PRS}$ . The black dots over the timeline shows the times the STP error is higher*  
835 *than  $\epsilon_{PRS}$*   
836

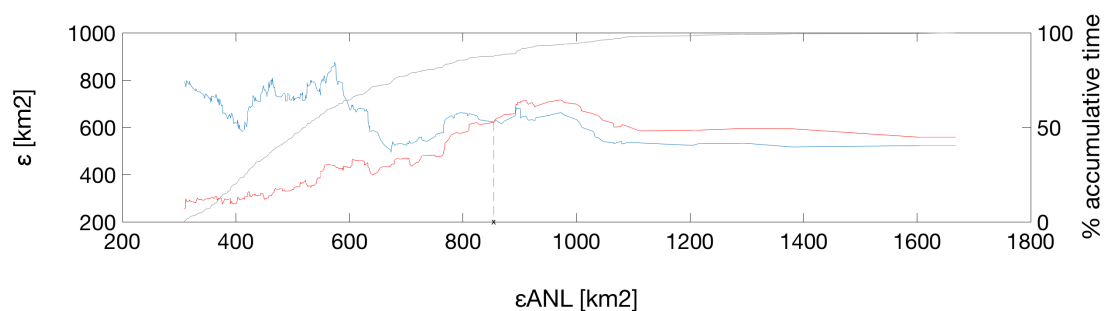


837  
838  
839



840 *Figure 5: X axis shows the  $\epsilon_{ANL}$ , ordered from minimum to maximum, for the winner*  
841 *analogue for the test year 2015. Left Y axis indicates  $\epsilon_{STP}$  (red) and  $\epsilon_{PRS}$  (blue) for*  
842 *the corresponding  $\epsilon_{ANL}$ . Right Y axis indicates the % of the accumulative comparison*  
843 *times as shown by the black solid line. Dashed vertical line indicates the crossing*  
844 *point between  $\epsilon_{STP}$  and  $\epsilon_{PRS}$  ( $\epsilon_{ANL}=853\text{Km}^2$ ).*

845



846

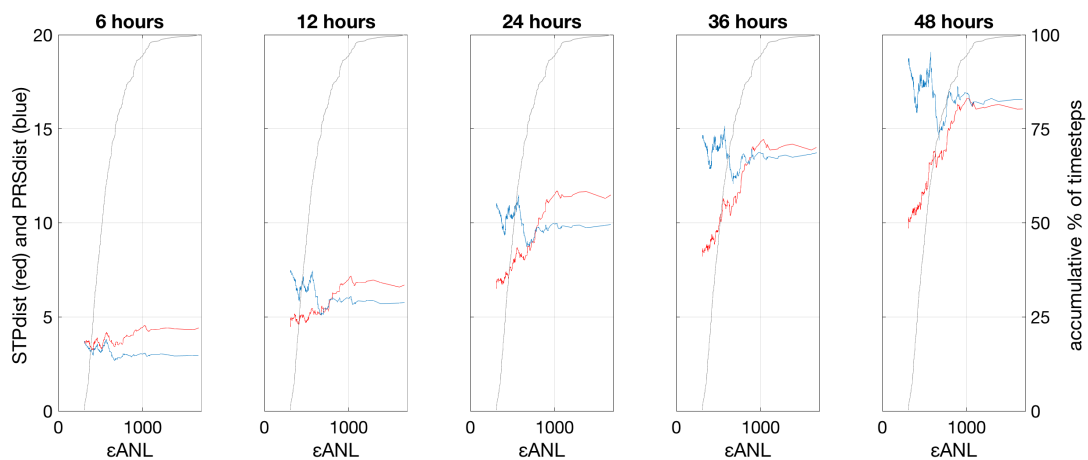
847

848



849 *Figure 6: Left Y axis indicates  $STP_{dist}$  (red) and  $PRS_{dist}$  (blue) for the corresponding*  
850  *$\epsilon_{ANL}$ , after 6, 12, 24, 36 and 48 hours. Right Y axis is the cumulative % of timesteps*  
851 *in the computation of the mean errors, as indicated by the black line in the plots. X*  
852 *axis is the  $\epsilon_{ANL}$ , ordered from minimum to maximum, for the winner analogue for the*  
853 *test year 2015.*

854



855

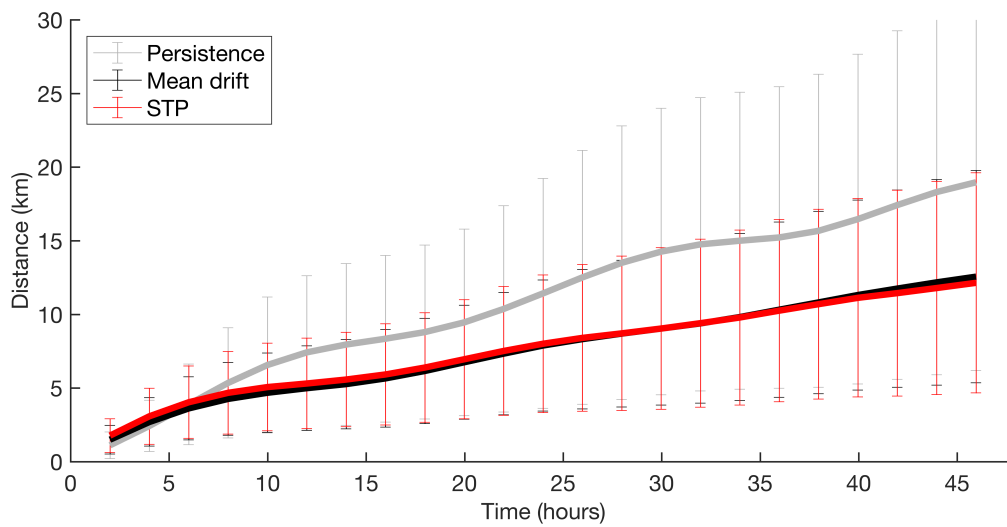
856

857



858 *Figure 7: Time evolution of the mean separation distances [km] between realized*  
859 *and forecast trajectories using realized and STP currents and the mean drift, with*  
860 *BoB system data, for 2015.*

861

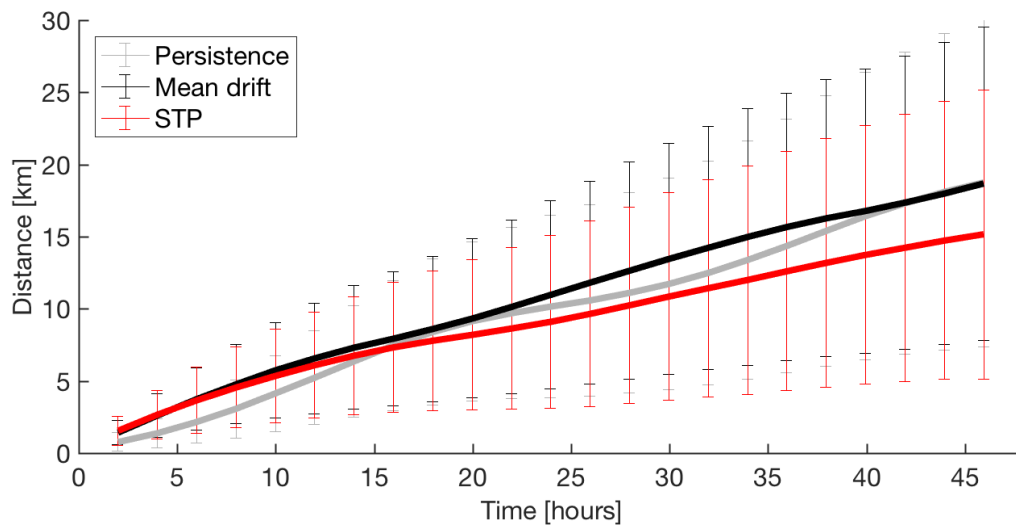


862

863



864 *Figure 8: (UP) Time evolution of the mean separation distances [km] between real*  
865 *and forecast trajectories using realized and STP currents and the mean drift, with*  
866 *the Red Sea HFR system data, for July 2017 to October 2018.*



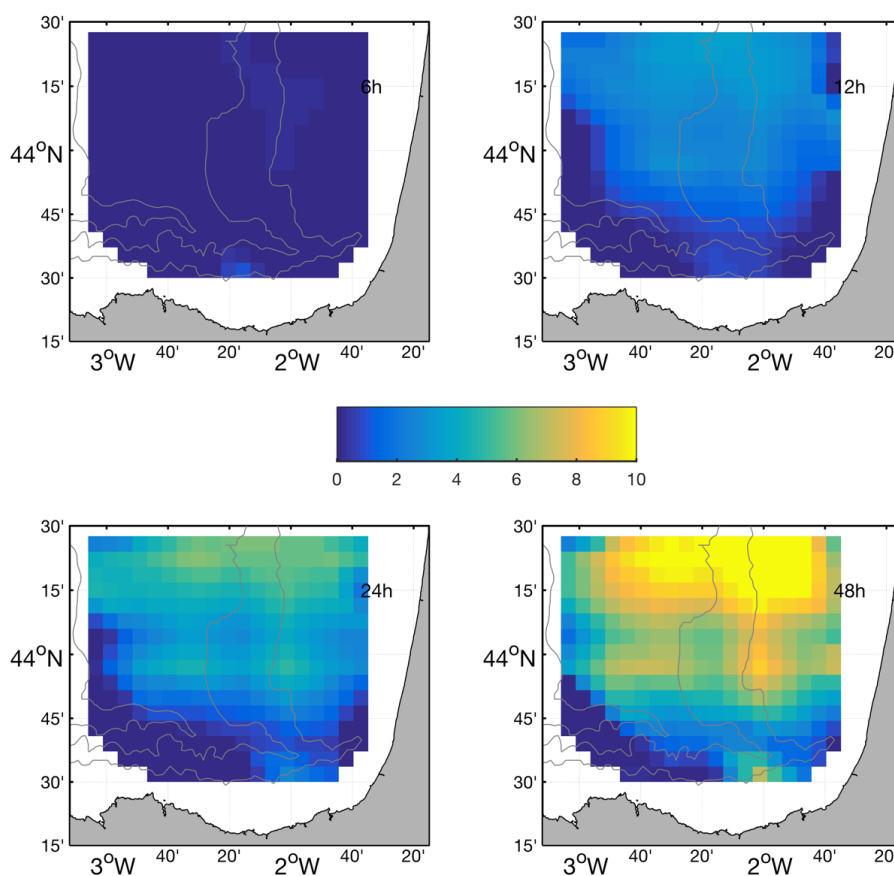
867

868

869



870 *Figure 9: Spatial distribution of separation distances [km] between trajectories*  
871 *using L-STP and persistent currents at 6, 12, 24 and 48 hours, for the BoB HFR*  
872 *System.*



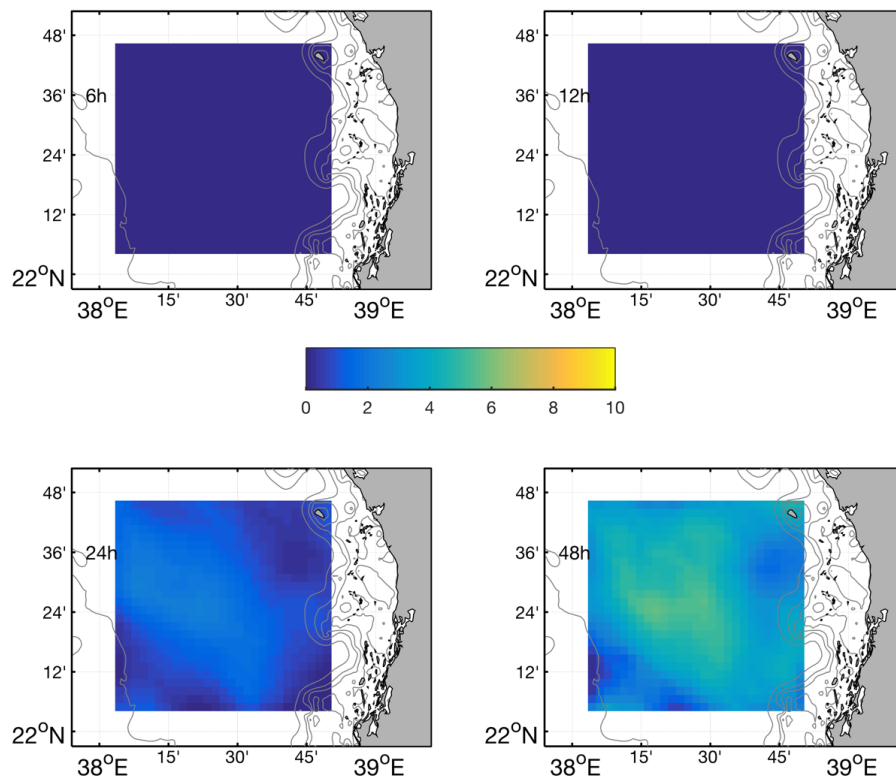
873

874

875



876 *Figure 10: Spatial distribution of separation distances [km] between trajectories*  
877 *using L-STP and persistent currents at 6, 12, 24 and 48 hours, for the Red Sea HFR*  
878 *system.*



879